Chem

CellPress

Research Article

Hydrogen Sensors from Ultra-small Bimetallic Nanoparticle Porous Ion Exchange Polymer Composites

Won-Tae Koo,[1,2] Yoonseob Kim,[3,4] Sunwoo Kim,[5] Bong Lim Suh,[6] Suchol Savagatrup,[3,7] Jihan Kim,[8] Sung-Ju Lee,[5] Timothy M. Swager,[3]* and Il-Doo Kim[1,2,9]*

[1]Department of Materials Science and Engineering, Korea Advanced Institute of Science and Technology, 291 Daehak-ro, Yuseong-gu, Daejeon 34141, Republic of Korea
[2]Advanced Nanosensor Research Center, KAIST Institute for Nanocentury, 291 Daehak-ro, Yuseong-gu, Daejeon 34141, Republic of Korea
[3]Department of Chemistry, Massachusetts Institute of Technology, Cambridge, Massachusetts 02139, United States
[4]Department of Chemical and Biological Engineering, Hong Kong University of Science and Technology, Clear Water Bay, Kowloon, Hong Kong SAR, China
[5]School of Computing, Korea Advanced Institute of Science and Technology, 291 Daehak-ro, Yuseong-gu, Daejeon 34141, Republic of Korea
[6]Materials and Life Science Research Division, Korea Institute of Science and Technology Seoul 02792, Republic of Korea
[7]Department of Chemical and Environmental Engineering, University of Arizona, 1133 E. James E. Rogers Way, Tucson Arizona 85721
[8]Department of Chemical and Biomolecular Engineering, Korea Advanced Institute of Science and Technology, 291 Daehak-ro, Yuseong-gu, Daejeon 34141, Republic of Korea
[9]Lead Contact
*Correspondence: idkim@kaist.ac.kr (I.-D.K.) and tswager@mit.edu (T.M.S.)

SUMMARY

Bimetallic nanoparticles (BM-NPs) have attracted much attention in catalysis, sensing, and electronics, as a result of their ultrahigh activity for surface reactions. For reliable utilization of BM-NPs in various applications, robust synthetic methods for the creation of non-aggregated functional BM-NPs with diameters less than a few nanometers are needed. Herein, we present functional assemblies of ultra-small BM-NPs produced within high stability porous ion exchange polymers. Specifically, PdPt NPs can be readily produced with precision dimensional control down to 1 nm. These PdPt NPs with porous polymers display superior hydrogen (H_2) sensing properties at room temperature in air. We achieve an ultra-low limit of detection (H_2 0.4 ppm), thereby confirming the outstanding sensing performance of the PdPt NPs. We further demonstrate a wireless H_2 sensing system by combining porous polymer-templated PdPt NPs with a radio-frequency identification (RFID) system, which enables the wireless detection of H_2 in a sealed gas head space.

Keywords: bimetallic nanoparticles, porous ion exchange polymers, hydrogen, sensors, wireless sensing

INTRODUCTION

Hydrogen (H_2) is an attractive renewable medium to store energy. It can be produced by electrolysis of water (H_2O), has high energy density per weight, and water is the exclusive byproduct with the release of stored energy.[1] However, H_2 is highly flammable gas and can explode in air at concentrations as low as 4%. Considering the fact that H_2 is odorless and colorless, H_2 gas leaks must be detected for safety. To detect H_2, various types of H_2 sensors, such as electrochemical, mechanical, and optical, and chemiresistive sensors, have been developed.[2] For instance, semiconducting metal oxides have been extensively investigated for chemiresistive H_2 sensors.[3] In addition, there is a significant advance in optical H_2 sensors by using metal-polymer composites that enable ultrafast H_2 detection.[4] However, their sensing systems are rather complicated, such as the needs of heaters for metal oxides and light sources/detectors for optical sensors, and further enhancement in H_2 sensing performances is required. On the other hand, Pd-based chemiresistors are well-known as an efficient H_2 sensor due to their simple sensing system, room temperature (r.t.) operation, low cost of sensor fabrication, and high H_2 selectivity.[5] The transduction involves a reaction between H_2 and Pd to produce the more resistive palladium hydride (PdH_x).[6] Specifically, the resistivity of $PdH_{0.7}$ is 2-fold higher than that of Pd. However, when operated in air, the H_2 reaction on Pd is retarded by adsorbed oxygen,[7] which lowers sensing response, sensing speed, and the detection limits. Existing solutions to address this issue include the

minimization of surface adsorbed oxygen[8] and the promotion of H_2 reactions by surface functionalization[9] or by alloying Pd with other elements.[10-12] However, the negative effect of oxygen remains unsolved and therefore the detection of sub-parts per million (ppm)-levels of H_2 in air remains an unmet challenge.

Bimetallic NP (BM-NPs) are an attractive solution to overcome these challenges, because BM-NPs are known to have superior activity for surface reactions relative to single-element metal NPs.[13–15] In some cases, synergistic effects are achieved by combinations of elements, which exceed the intrinsic properties of each individual element.[16] Thus, we hypothesized that the combination of Pd with Pt could be complementary for H_2 sensing in air, as a result of the fact that platinum (Pt) is also able to detect H_2 by reactions that remove surface adsorbed oxygen.[17] In addition, it has been demonstrated that alloying with Pd and Pt into BM-NPs with a diameter of 7.2 nm increases the H_2 storage capacity significantly as compared to pristine Pd NPs.[18] The chemical and physical properties of BM-NPs are strongly correlated with their structure, size, and composition. It is known that BM-NPs have exceptionally high catalytic activity when their size is kept below a few nanometers as a result of unsaturated surface states.[19,20] These high energy surfaces produce intrinsic instability and particle fusion is problematic. Hence, producing ultra-small BM-NPs that are not prone to agglomeration is critical to maintain this activity. Prior methods to stabilize/immobilize PdPt NPs include the impregnation into supports,[21] chemical reduction,[22] polyol method,[23] electrochemical deposition,[24] and laser ablation.[25] Nevertheless, these methods not only often produce PdPt NPs having a large average size and broad size distributions but also face challenges such as complicated processes, high processing costs, or low yields. In addition, it is difficult to control the optimal loading ratio of respective elements into BM-NPs while maintaining their size to sub-nm scale (the detailed pros/cons are summarized in **Table S1**). These limitations have hindered the practical usage of BM-NPs in various applications including chemical sensors.

Herein, we report a facile synthesis of BM-NPs by using porous ion exchange polymers to create high performance H_2 sensors that enable wireless detection. The ability to precisely tune the size and composition of BM-NPs is critically important to the sensory performance. This control is afforded by the use of a porous ion exchange polymer, which enables homogeneous diffusion and immobilization of ionic metal precursors of complementary charge into the polymer matrix. Chemical reduction to generate NPs within the rigid porous matrix generates a material with high gas permeability and suppresses growth of NPs in size.[26] The result is a robust convenient method to create ultra-small (down to 1 nm) well-dispersed BM-NPs in the porous polymer matrix. PdPt NP-based H_2 sensors exhibit improved H_2 sensing properties at r.t. in air, as a result of the high and unique activity of bimetallic PdPt NPs, which display both hydrogen adsorption and oxygen removal reactions. The limit of detection (LOD) for the H_2 sensors is 0.4 ppm, and new sensing mechanisms are described. Furthermore, the sensor systems can be paired with a radio-frequency identification (RFID) system to detection of H_2 in a sealed gas head space.

RESULTS AND DISCUSSION

Structural Design and Characterizations

Figure 1 illustrates the polymer synthesis, fabrication of PdPt NPs *via* ion exchange in a porous ionic polymer, and the application as chemireisitve H_2 sensors. Imidazolium-functionalized triptycene polyether sulfone (ITPES) as a porous cationic polymer is synthesized by chloromethylation of TPES and nucleophilic substitution reaction (**Figure 1A**), as reported previously.[27,28] The structure of ITPES is confirmed by ^{1}H-NMR (**Figure S1**). Drop-coating (10 μL) of ITPES (1 mg 1 mL^{-1} in methanol) produces an ITPES-matrix on a substrate with an average thickness of 50 nm (**Figure S2**). Aqueous $PdCl_4^{2-}$ and $PtCl_4^{2-}$ solutions (3.063 mM and 2.409 mM, respectively) are deposited on the polymer films and these ions displace the chloride ions in ITPES. Lastly, PdPt NPs are produced by $NaBH_4$ reduction (**Figure 1B**, see details in the Supplemental Information). The free volume imposed by the triptycene creates an ITPES-membrane with highly porous structure,[29] and the size of PdPt NPs is restricted by the matrix. By using this method, ITPES-PdPt NPs can

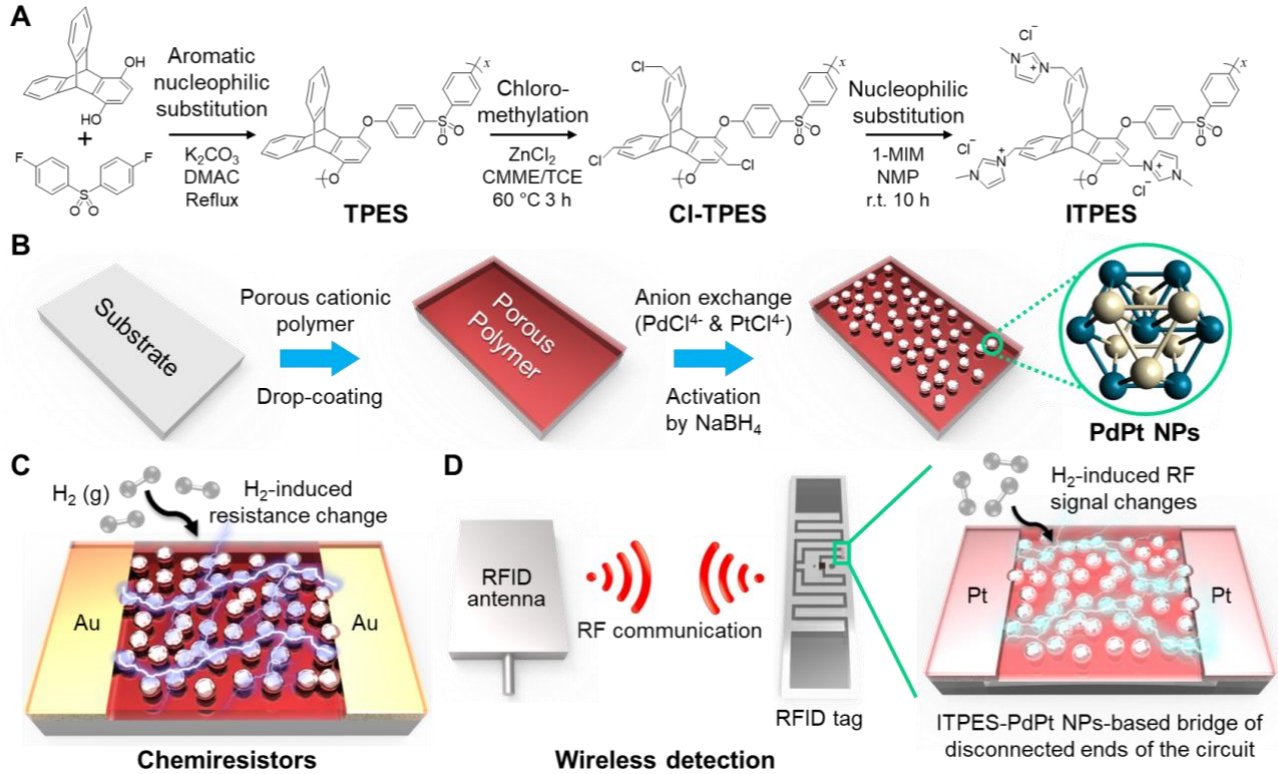

Figure 1. M-NP porous ion exchange polymer composites and chemiresistive H_2 sensing system with wireless detection.

(A) Schematic illustration of the synthesis of ITPES.

(B) Schematic illustration of the preparation of ITPES-PdPt NPs.

(C) Schematic illustration of ITPES-PdPt NPs-based chemiresistors.

(D) Schematic illustration of ITPES-PdPt NPs-based wireless sensors.

be deposited on glass (SiO_2), alumina (Al_2O_3), and polyethylene terephthalate (PET) film, for chemiresistive (**Figure 1C**) and wireless sensing (**Figure 1D**).

The size and distribution of PdPt NPs is controlled by the $PdCl_4^{2-}$ and $PtCl_4^{2-}$ loading and the total volume of aqueous solutions used in the ion exchange. As shown in **Figure 2A**, ultra-small PdPt NPs are formed when 10 μL of metal precursors are spread over an area of ~30 mm^2. The resulting 1.07 ± 0.56 nm PdPt NPs are isolated from each other in the porous polymer (ITPES)-matrix (**Figure 2B and Figure S3A**). The increased lattice period (0.230 nm) of PdPt (111) plane is observed compared with that of Pd (0.225 nm for (111), JCPDS no. 46-1043) and Pt (0.226 nm for (111), JCPDS no. 04-0802) (**Figure 2C**, **Figure S4** and **S5**). The increased lattice fringe of PdPt NPs was also observed in the previous studies.[30] Increased loading amounts of metal anions to 20 μL, produced 1–5 nm PdPt NPs with a percolated network (**Figure 2D and Figure S3B**). As a result of the free volume constraints of ITPES, the aggregation of PdPt NPs is minimized and the size of most PdPt NPs is limited in a few nanometers. The Cs-corrected scanning transmission electron microscopy (STEM) image of the larger particles also shows the well-dispersed NPs (**Figure 2E**) and the lattice fringe of (111) plane of PdPt NPs also increased to 0.232 nm (**Figure 2F**). The energy-dispersive X-ray spectroscopy (EDS) elemental mapping images are consistent with PdPt NPs dispersed in ITPES-matrix. The matrix is uniform as evidenced by the C, N, S, and O maps (**Figure 2G**). The EDS line profile analysis of the blue line in Figure 2e further confirms that Pd and Pt are homogeneously distributed within in PdPt NPs (**Figure 2H**). However, without the use of ITPES, the same synthetic process produced film-like PdPt structure (PdPt films) as a result of PdPt NP aggregation during the activation process (**Figure S6**). EDS elemental mapping analysis also reveals a non-homogeneous structure of PdPt films (**Figure S6**). These results clearly confirm that anion exchange porous polymer-matrix method is a facile and controllable route to ultra-small and well-dispersed BM-NPs on a substrate.

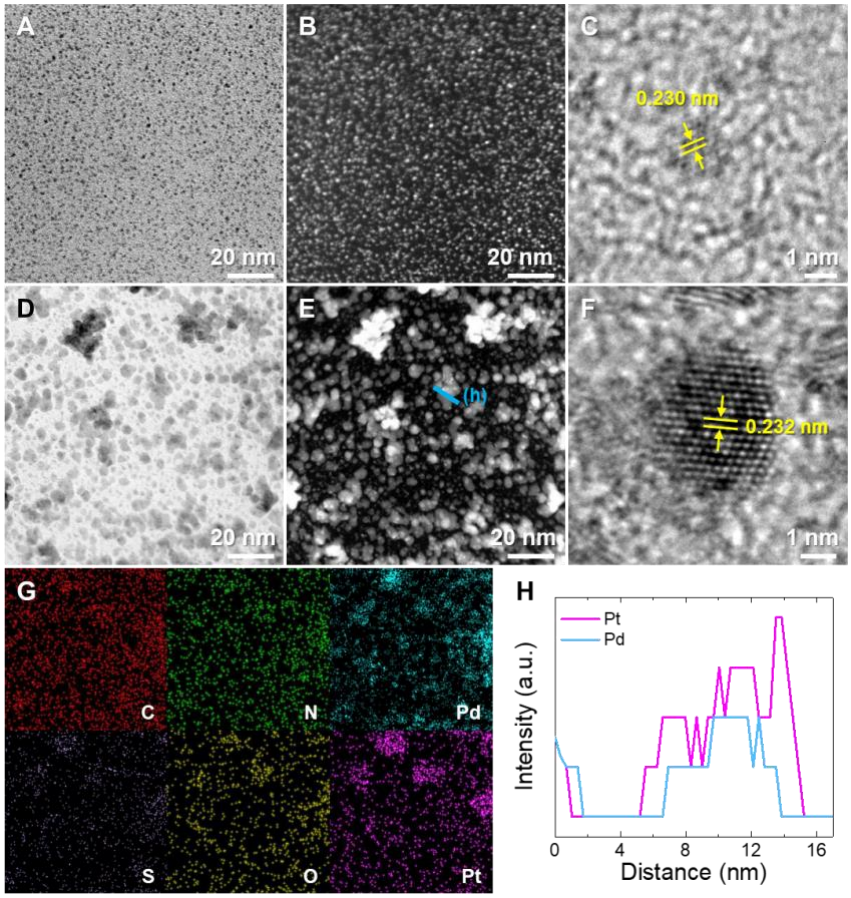

Figure 2. TEM analysis of ITPES-PdPt NPs.
(A–F) ITPES-PdPt NPs prepared by the drop-coating of Pd and Pt anions with a total volume of (A–C) 10 μL and (D–F) 20 μL. (A and D) TEM images, (B and E) STEM images, and (C and F) high-resolution TEM images.
(G) EDS elemental mapping analysis corresponding to the region of Figure 2E.
(H) EDS elemental line profiles of the blue line in Figure 2E.

Ex-situ ultraviolet-visible (UV-Vis) spectra confirm the conversion $PdCl_4^{2-}$ and $PtCl_4^{2-}$ to NPs in the porous polymers after $NaBH_4$ reduction (**Figure S7**). Prior to reduction broad absorbance spectra at 325 nm and 230 nm are indicative of $PdCl_4^{2-}$ and $PtCl_4^{2-}$ in the ITPES-matrix.[31,32] The $PdCl_4^{2-}$ absorbance spectra are absent after $NaBH_4$ reduction and a new metal NP resonance is present at the location of the $PtCl_4^{2-}$ peak. The attenuated total reflection-Fourier-transform infrared (ATR-FTIR) spectra of ITPES-PdPt NPs match with pristine ITPES (**Figure S8A**), confirming that the chemical integrity of the polymer is maintained. X-ray diffraction (XRD) analysis of ITPES-PdPt NPs displays the weak peaks at 40° (**Figure S8B**), which position is similar to the XRD PdPt film patterns (**Figure S9**). To further support the formation of bimetallic PdPt NPs in ITPES, we conducted X-ray photoelectron spectroscopy (XPS) analysis of ITPES-PdPt NPs relative to monometallic control samples ITPES-Pd NPs and ITPES-Pt NPs, as well as films of Pd, Pt, and PdPt synthesized by the same conditions without ITPES. In the PdPt NPs, the Pd 3d and Pt 4f peaks are shifted to low binding energy as compared to the control samples (**Figure 3A and 3B**). The Pd and Pt phases separate in PdPt films, and the peaks in the PdPt NPs are shifted from those observed in the films (from 335.3 eV for Pd $3d_{5/2}$[33] to 334.9 eV and from 71.0 eV for Pt $4f_{7/2}$[34] to 70.7 eV). These peak shifts demonstrate the formation of BM-NPs and are consistent with reported previously results.[35,36] In addition, the high-resolution XPS spectra of C 1s, N 1s, and S 2p confirm C–C, C–O, and C–N bonds,[37] imidazolium,[38] and sulfone groups[39] (**Figure S10–S12**), demonstrating the existence of intact ITPES in each of the ITPES-PdPt NP, ITPES-Pd NP, and ITPES-Pt NPs compositions.

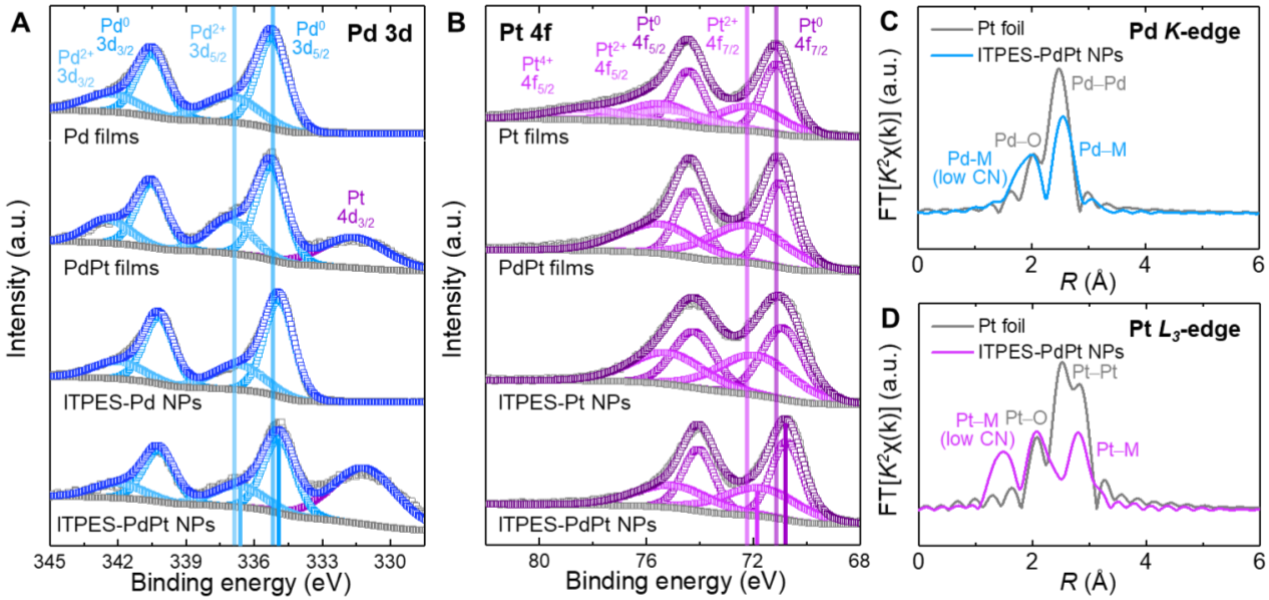

Figure 3. High-resolution XPS and EXAFS spectra of the samples.
(A) XPS spectra of Pd films, PdPt films, ITPES-Pd NPs, and ITPES-PdPt NPs in the vicinity of Pd 3d. (B) XPS spectra of Pt films, PdPt films, ITPES-Pt NPs, and ITPES-PdPt NPs in the vicinity of Pt 4f.
(C) The fitted EXAFS spectra of Pd foil and ITPES-PdPt NPs at the Pd *K*-edge.
(D) The fitted EXAFS spectra of Pt foil and ITPES-PdPt NPs at the Pt L_3-edge.

The formation of bimetallic PdPt NPs is further supported by X-ray absorption spectroscopy (XAS) analysis. The X-ray absorption near edge structure (XANES) spectra of ITPES-PdPt NPs indicate the metallic state of Pd and Pt (**Figure S13**). The slight shifts of the white line peaks in both the Pd *K*-edge and Pt L_3-edge XANES spectra are resulted from the surface adsorbed oxygen on Pd and Pt elements.[40] We also fitted the Fourier transforms of extended X-ray absorption fine structure (EXAFS) spectra of the samples to investigate atomic bonding states in the ITPES-PtPd NPs (**Figure S14 and S15**). Both Pd *K*-edge and Pt L_3-edge EXAFS spectra show the new peak at 1.0–2.0 Å and Pd–M (M = Pd or Pt) and Pt–M bonding at 2.0–3.0 Å compared with those of references (**Figure 3C and 3D**). These new peaks are related to surface oxygen bonding or metal–metal bonding having a low coordination number (CN).[41] In addition, the EXAFS fit parameters confirm the presence of Pt–Pd and Pd–Pt bonding and the decreased total CN of ITPES-PdPt NPs (9.9 for Pd and 8.8 for Pt, and 12 for reference foils) (**Table S2**). These results clearly demonstrate the formation of ultra-small bimetallic PdPt NPs, which are consistent with TEM and XPS analysis.

Sensing Characteristics of ITPES-PdPt NPs

To probe the activity of ITPES-PdPt NP to detect hydrogen, we fabricated chemiresistors (see the Supplemental Information for details). Unfortunately, 1 nm-sized ITPES-PdPt NPs did not display sufficient electrical conductivity, however with increased loading metal precursor loading, ITPES-PdPt NPs exhibited a percolated network and electrical conductivity.[42] To optimize the system we varied the molar ratio of Pd to Pt in PdPt NPs to $Pd_{0.75}Pt_{0.25}$, $Pd_{0.67}Pt_{0.33}$, $Pd_{0.5}Pt_{0.5}$, and $Pd_{0.33}Pt_{0.67}$, through the loading of the Pd and Pt precursors (**Figure S16**). The sensing tests were conducted at r.t. in air and $Pd_{0.5}Pt_{0.5}$ NPs exhibited the best sensing properties. In these investigations, we investigated the H_2 sensing properties of different ITPES-PdPt NPs as well as the control samples: ITPES-Pd NPs, ITPES-Pt NPs, and PdPt films. ITPES-PdPt NPs exhibit significant resistive responses for exposures of 1–4% of H_2 (**Figure 4A**), and a normalized response ($|\Delta R/R_a|$) to 4% H_2 is 16.0%. In contrast, the PdPt films show lower resistance changes and a response ($|\Delta R/R_a|$) of 0.53% to 4% H_2. The reasons for the baseline drift after H_2 exposures is not clear, however similar drifts were observed in previous studies.[8,10] ITPES-Pd NPs and ITPES-Pt NPs also display increased H_2 responses relative to the PdPt films, with H_2 [4%] responses ($|\Delta R/R_a|$) of 6.78% and 5.09% for ITPES-Pd NPs and ITPES-Pt NPs respectively, confirming

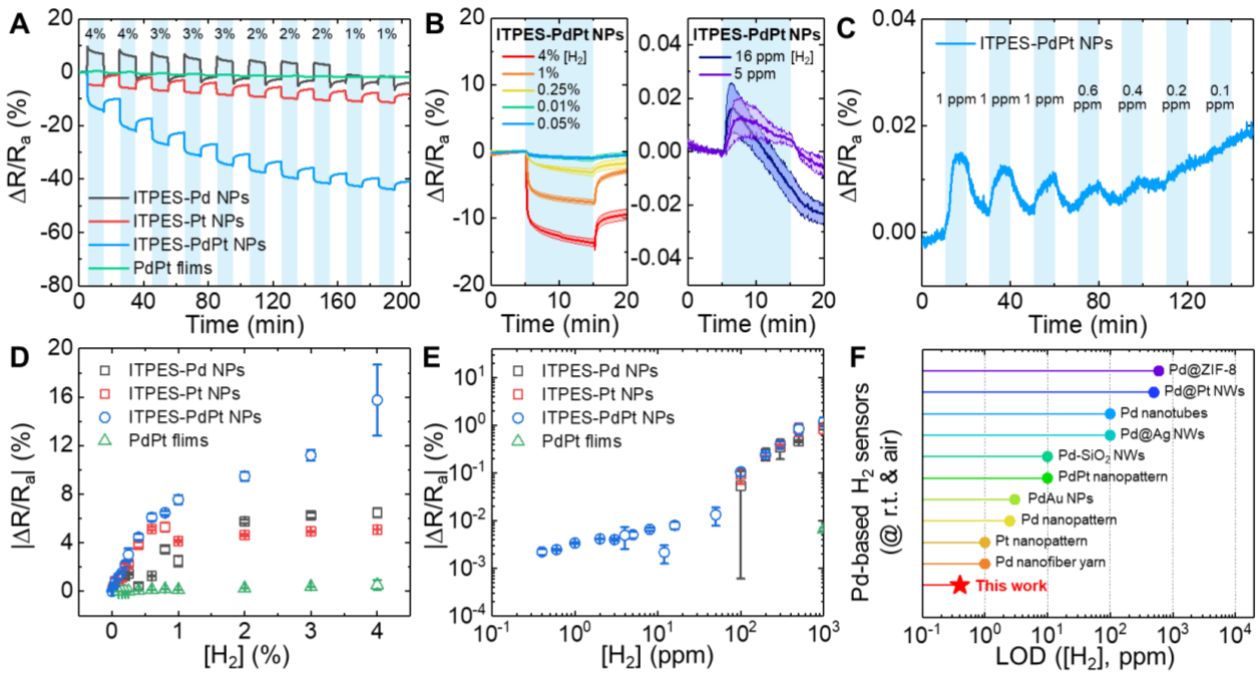

Figure 4. Sensing characteristics of the samples.

Sensing characteristics of ITPES-Pd NPs, ITPES-Pt NPs, ITPES-PdPt NPs, and PdPt films at r.t. in air. (A–C) Response traces of the sensors: (A) in the range of 1–4% of H_2, (B) to 5 and 16 ppm, and 0.05, 0.01, 0.25, 1, and 4% of H_2, and (C) in the range of 0.1–1 ppm of H_2.

(D and E) Normalized responses of the sensors to (D) high levels of H_2 and (E) low levels of H_2.

(F) Comparison of H_2 detection limits of Pd-based H_2 sensors.

the fact that NPs increase activity. ITPES-PdPt NPs, ITPES-Pd NPs, and ITPES-Pt NPs are all capable of detecting 0.01–0.8% of H_2, however the PdPt films will not function at these low concentrations (**Figure S17**). The triplicate response traces of ITPES-PdPt NPs-based sensors display stable resistance changes to repeated 0.8% H_2 exposures of 10 h (**Figure S18A**), demonstrating high reproducibility and stability. In addition, the ITPES-PdPt NPs show stable response traces after storage in ambient air for 1–3 months, although the 4% H_2 $|\Delta R/R_a|$ decrease to 6.95% after 1-month, 4.67% after 2-months, and 4.50 after 3-months (**Figure S18B and S18C**).

The resistance for the ITPES-PdPt NPs sensors decreased when exposed to H_2 concentrations over 100 ppm (**Figure 4B** and **Figure S17**) and then switches to an increase in resistance with H_2 exposures below 16 ppm (**Figure 4B** and **Figure S19**). This switchover is the result of reactions at high H_2 concentrations to liberate surface oxygen species that are generating interparticle resistance. The ITPES-PdPt NPs enable trace H_2 detection to 0.4 ppm (**Figure 4C**), which is superior to the limits of detection of 100 ppm for ITPES-Pd NPs and ITPES-Pt NPs, and 0.1% for PdPt films (**Figure S17** and **S20**). The sensor responses H_2 concentrations are summarized in **Figure 4D and 4E**. ITPES-PdPt NPs show the highest response to 1% H_2 of 7.56% and the other responses are 2.50% for ITPES-Pd NPs, 4.15% for ITPES-Pt NPs, and 0.13% for PdPt films. In addition, the time to obtain a 90% response (t_{90}) is accelerated from 386 s for PdPt films to 92 s at ITPES-PdPt NPs for the detection of H_2 1% and the recovery time to 10% of the total response (t_{10}) also reduced from 476 s to 304 s (**Figure S21**). The ITPES-PdPt NPs are selective for H_2 with minimal cross-response to interfering gases such a NO_2, NO, CO, NH_3, HCHO, and C_2H_5OH (**Figure S22**). Furthermore, the ITPES-PdPt NP sensor response of 11.0% to 2% H_2 in 50% relative humidity air, is very similar to 11.2% measured in dry air (**Figure S23**). These results confirm the feasibility of ITPES-PdPt NPs as a selective and stable H_2 sensor. **Figure 4F** shows the comparative limits of detection (LOD) of our system with other Pd-based H_2 sensors operated at r.t. in air, as reported in recent literature (see the summary in **Table S3**).[4,8–10,43–51] As shown, although the response times are not fast, the ITPES-PdPt NPs sensors show a superior H_2 LOD as compared to previous Pd-based H_2 sensors.

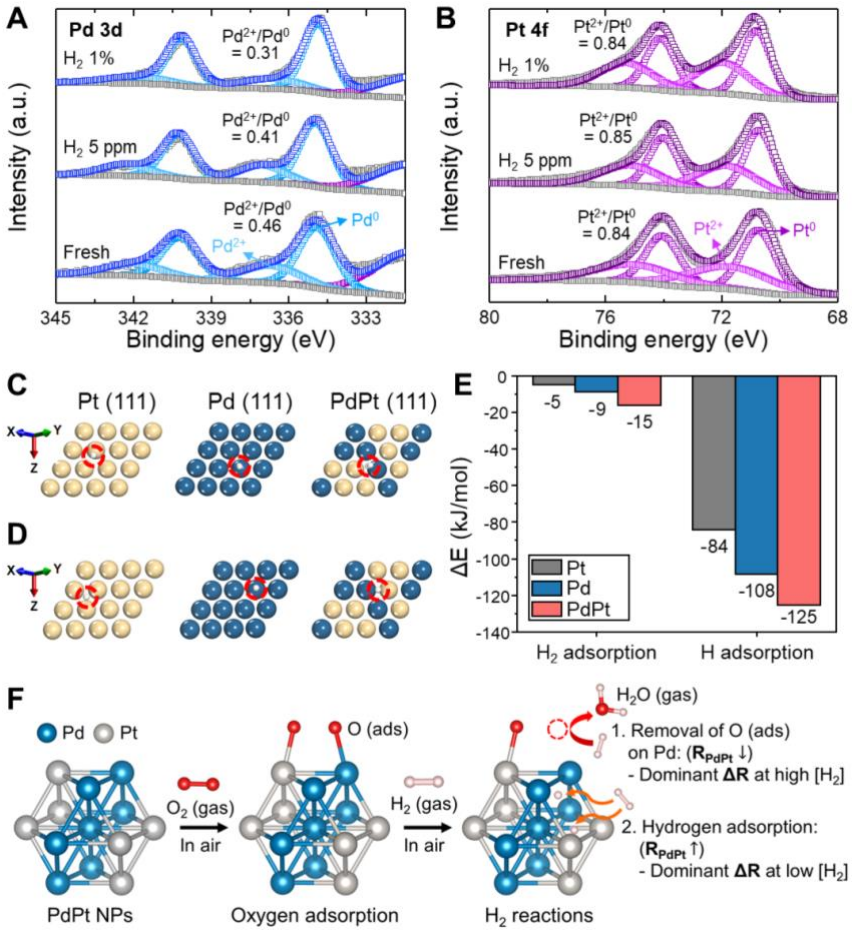

Figure 5. Investigation of sensing mechanisms of ITPES-PdPt NPs.

Sensing mechanisms of ITPES-PdPt NPs at r.t. in air.

(A and B) *Ex-situ* XPS spectra after exposures of 5 ppm and 1% of H_2 in the vicinity of (A) Pd 3d and (B) Pt 4f.

(C and E) Density functional theory (DFT) calculations; (C) Top views of the optimized structures of an adsorbed H_2 (red circles) on the (111) surface of Pt, Pd, and PdPt NPs. (D) Same as (C) but with adsorbed H (red circles) on the (111) surfaces of NPs. (E) Calculated binding energies for the adsorption of H_2 and H on the surface of Pt, Pd, and PdPt NPs.

(F) Schematic illustration of the H_2 sensing mechanisms of ITPES-PdPt NPs.

Hydrogen Sensing Mechanisms of ITPES-PdPt NPs

We carried out *ex-situ* XPS analysis to elucidate the H_2 sensing mechanism of ITPES-PdPt NPs detailing (1) H_2 adsorption at low [H_2] and (2) the removal of surface adsorbed oxygen at high [H_2]. The ITPES-PdPt NPs-based sensors were exposed to 5 ppm and 1% of H_2 for 10 min before XPS measurements (**Figure 5A and 5B**). The ratio of Pd^{2+} to Pd decreases after H_2 exposures, while the ratio of Pt^{2+}/Pt is unchanged. These ratio changes suggest that the oxygen adsorbed on PdPt NPs is removed by H_2 and that the reaction dominantly occurs at Pd sites. The oxygen reduction that is occurred on Pd sites is consistent with the catalytic water formation on the Pd surfaces.[9] Thus, the *ex-situ* XPS results support (i) the atomically distributed PdPt NPs and (ii) that reductive release of surface oxygen at higher concentrations of H_2 leads to a decrease in the resistance of PdPt NPs. The sensing tests in oxygen-free atmospheres (N_2 balance) further support our hypothesis (**Figure S24**). ITPES-Pd NPs and ITPES-PdPt NPs sensors show increase of resistances for exposures of 0.1 ppm to 4% of H_2 with the ITPES-Pd NPs devices having much larger responses. In contrast, the ITPES-Pt NPs-based sensors that lack Pd didn't display noticeable responses. Thus, we confirm that the nanoscopic Pd or PdPt dramatically promote H_2 reactions due to their nanosize effect. However, compared to the H_2 sensing properties in air, the LOD of ITPES-Pd NPs are severely degraded from 0.1 ppm for N_2 atmospheres to 100 ppm for air, because adsorbed oxygen on Pd retards H_2 reactions with Pd.[7] On the other hand, ITPES-PdPt NPs 1) induce more increased

hydrogen adsorption in air due to the bimetallic synergies of PdPt[10] and 2) translate oxygen reactions with hydrogen on PdPt NPs into signals of chemiresistors. Therefore, their excellent sensing properties remain even in air operation (H_2 LOD: 0.1 ppm for N_2 and 0.4 ppm for air).

To further demonstrate the bimetallic synergies of PdPt NPs on H_2 sensing, we conducted density functional theory (DFT) calculations. We calculated (1) molecular H_2 adsorption energies and (2) dissociative H_2 adsorption (H adsorption) on the dominant surface plane of Pd, Pt, and PdPt NPs. **Figure 5C and 5D** show the optimum structures for the adsorption of H_2 and H (red circles in **Figure 5C and 5D**) on (111) facet of Pt, Pd, and PdPt. The calculated binding energies for H_2 adsorption are –5.02 kJ/mol on Pt, –9.31 kJ/mol on Pd, and –15.12 kJ/mol on PdPt, and the H adsorption energies are –83.95 kJ/mol on Pt, –108.22 kJ/mol on Pd, and –125.48 kJ/mol on PdPt (**Figure 5E**). These binding energies indicate that the adsorption of H_2 and H has a stronger preference for the PdPt surfaces as opposed to pure ones. These results are well matched with previous studies on H_2 adsorption on Pd–Pt alloy.[10,52–54] The hybridization of d-orbitals of Pd and Pt atoms in vacuum or in ambient air induces the downshift of the d-band center of Pt, lowering the adsorption energy of H_2 on Pd/Pt interfaces. Thus, PdPt NPs lead to synergetic H_2 adsorption properties, which is in good agreement with our sensing results.

From these results, we conclude the H_2 sensing mechanisms of ITPES-PdPt NPs as follows (**Figure 5F**). When PdPt NPs are exposed to H_2, there are two reactions that occur: (1) the removal of surface adsorbed oxygen giving a decrease in resistance and (2) hydrogen adsorption resulting in an increase in resistance. Both reactions occur simultaneously, but the former dominants the resistance at high levels of [H_2] and the latter at low levels of [H_2]. Therefore, the detection limits and responses of the sensors are hugely increased but response times are not accelerated.

Wireless Hydrogen Sensing System

To take advantage of our method that can easily apply to various substrates, we further developed wireless H_2 sensing systems by combining ITPES-PdPt NPs with an RFID system. The ITPES-PdPt NPs were directly deposited on a conventional RFID tag with the same synthetic process used in the chemiresistor fabrication. To translate the chemiresistive sensing behaviors of PdPt NPs to signals in RF communications, the ITPES-PdPt NPs bridged the disconnected ends of the RF resonant circuit. The ITPES-PdPt NPs-RFID tag was placed in the sealed chamber (**Figure 6A and 6B**) and the RFID antenna was positioned 4 cm above the tag in the chamber (**Figure 6C**). **Figure 6D** shows the traces of received signal strength (S_{11}) changes (ΔGain) of the ITPES-PdPt NPs-based wireless H_2 sensor. Because S_{11} is inversely proportional to circuit resistance,[55] ΔGain has a positive value as a result of the resistance decrease observed from the ITPES-PdPt NPs with exposure to 1–4% of H_2. The wireless H_2 sensor showed sensitive responses to H_2 with ΔGain = 1 dB at 4% H_2. The phase changes also indicate that ITPES-PdPt NPs wirelessly detected H_2 in real time (**Figure 6E**). Although the LOD (1%) of the wireless H_2 sensing system is lower than that (0.4 ppm) of the ITPES-PdPt NPs-based chemiresistors due to the noise signals in air and interferences with surrounding,[56] the chemiresistive behaviors of ITPES-PdPt NPs are successfully translated into RF communication signals. On the other hand, controls using the pristine RFID tag did not show any noticeable signals toward H_2 exposure (**Figure S25**). These results clearly demonstrate the realization of wireless H_2 sensing by hybridizing the ITPES-PdPt NPs sensing layer and RFID tag. Note that, because the wireless sensing system using our method is a proof-of-concept demonstration of the future sensing systems, we did not further optimize the wireless sensing performances. With the rational design of RF communication systems, the wireless H_2 sensing system is applicable to various fields, such as leakage detection in a sealed space, environmental monitoring, and drone sensors.

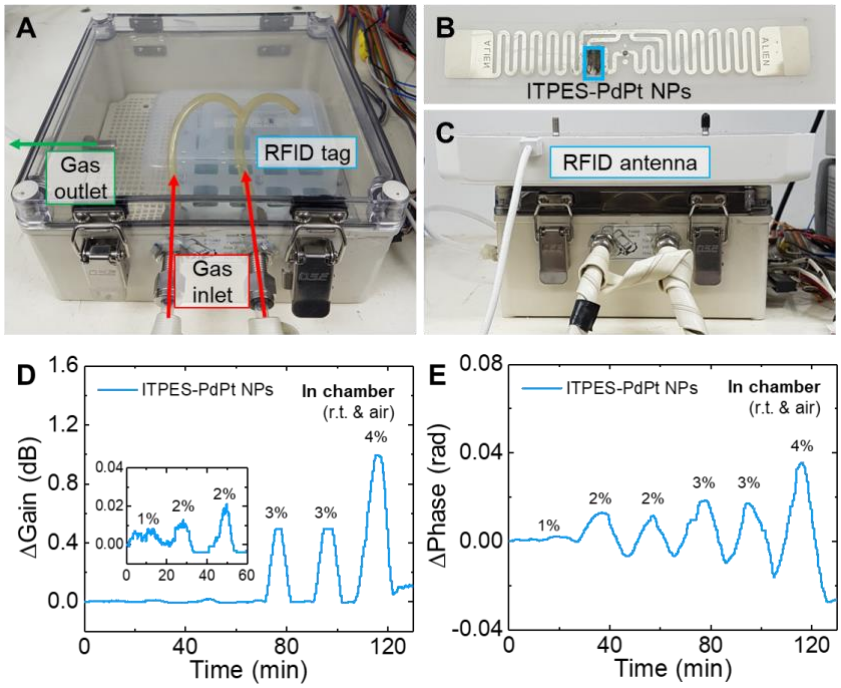

Figure 6. Photographs of the experimental set-up for wireless sensing tests and wireless sensing characteristics.

(A) Photograph of the RFID tag-embedded gas chamber. The RFID tag was attached to a holder.

(B) Photograph of the ITPES-PdPt NPs-deposited RFID tag. ITPES-PdPt NPs were deposited in the region of the blue box in Figure 5B.

(C) Photograph of a RFID antenna placed on the gas chamber. The distance between the RFID tag and RFID antenna was 4 cm.

(D) Dynamic changes of received signal strengths (S_{11}).

(E) Phase changes of ITPES-PdPt NPs-based wireless H_2 sensors to exposures of 1–4% of H_2.

In conclusion, we developed the facile synthesis method to create conductive networks of ultra-small BM-NPs by using anion exchange in the porous cationic polymers and subsequent reductive activation. The porous ion exchange polymers allow the facile diffusion of heterogeneous ionic metal precursors in the polymer matrix and also limit the growth of NPs, enabling the reproducible formation of highly active 1 nm scale BM-NPs. The porous polymer matrix also allows for gas accessibility to the BM-NPs. As a result of the superior activity of PdPt NPs, the ITPES-PdPt NPs-based sensor exhibited high stability and excellent H_2 sensing properties with a 15.7% response to 4% H_2 and a limit of detection of 0.4 ppm. The H_2 sensing mechanism of PdPt NPs in air was verified to be related to the two reactions: (1) the removal of surface adsorbed oxygen (decreased resistance) at Pd sites at the interfaces of Pd/Pt atoms and (2) hydrogen adsorption (increased resistance) within the PdPt NPs. Based on outstanding H_2 sensing performance, we further demonstrated the wireless sensing system, for detection of H_2 in a sealed head space, by combining RFID tag with ITPES-PdPt NPs. Our approach can be extended to i) diverse BM-NPs deposited onto various supports and ii) applications that require the superior activity of BM-NPs.

EXPERIMENTAL PROCEDURES

Full experimental procedures are provided in the Supplemental Information.

SUPPLEMENTAL INFORMATION

Supplemental Information can be found online at “https://doi.org/”. Supplemental Information includes experimental procedures, 25 figures, and three tables.

ACKNOWLEDGMENTS

This work was supported by Korea Electric Power Corporation (KEPCO) Research Institute, and by Wearable Platform Materials Technology Center (WMC) (No. 2016R1A5A1009926), and Energy Cloud R&D Program (NRF-2019M3F2A1072233) funded by National Research Foundation of Korea (NRF) Grant of the Korean Government (MSIT). This work was supported by the National Research Foundation of Korea (NRF) grant funded by the Korea government (MSIT) (No. 2020R1A2C301312711). This work was also supported by the National Science Foundation DMR-1809740. We thank Pohang Accelerator Laboratory (PAL) for the assistance in synchrotron XAS analysis.

AUTHOR CONTRIBUTIONS

W.-T.K. conceived the concept and designed experiments. Y.K. synthesized porous ion exchange polymers. W.-T.K. prepared the materials and conducted structural characterization and sensing measurements. W.-T.K. and S.K. performed wireless sensing measurements. S.S. assisted sensing measurements. S.-J.L. supported wireless sensing tests. B.L.S. and J.K. conducted DFT calculations. All authors contributed to the writing of the manuscript. All authors discussed the results and the manuscript. I.D.K. and T.M.S. were responsible for managing all aspects of this project.

DECLARATION OF INTERESTS

The authors declare no competing interests.

REFERENCES AND NOTES

1. Jacobson, M.Z., Colella, W., and Golden, D. (2005). Cleaning the air and improving health with hydrogen fuel-cell vehicles. Science *308*, 1901–1905.
2. Hübert, T., Boon-Brett, L., Black, G., and Banach, U. (2011). Hydrogen sensors–a review. Sens. Actuators, B. *157*, 329–352.
3. Sharma, B., Sharma A., and Kim. J.-S. (2018). Recent advances on H_2 sensor technologies based on MOX and FET devices: a review. Sens. Actuators, B. *262*, 758–770.
4. Nugroho, F.A., Darmadi, I., Cusinato, L., Susarrey-Arce, A., Schreuders, H., Bannenberg, L.J., Fanta, A.B.d.S., Kadkhodazadeh, S., Wagner, J.B., Antosiewicz, T.J. et al. (2019). Metal–polymer hybrid nanomaterials for plasmonic ultrafast hydrogen detection. Nat. Mater. *18*, 489–495.
5. Favier, F., Walter, E.C., Zach, M.P., Benter, T., and Penner, R.M. (2001). Hydrogen sensors and switches from electrodeposited palladium mesowire arrays. Science *293*, 2227–2231.
6. Lewis, F.A. (1967). The Palladium Hydrogen System. Academic Press, New York.
7. Yang, F., Kung, S.-C., Cheng, M., Hemminger, J. C., and Penner, R.M. (2010). Smaller is faster and more sensitive: The effect of wire size on the detection of hydrogen by single palladium nanowires. ACS Nano *4*, 5233–5244.
8. Koo, W.-T., Qiao, S., Ogata, A.F., Jha, G., Jang, J.-S., Chen, V.T., Kim, I.-D., and Penner, R.M. (2017). Accelerating palladium nanowire H_2 sensors using engineered nanofiltration. ACS Nano *11*, 9276–9285.
9. Li, X., Liu, Y., Hemminger, J.C., and Penner, R. M. (2015). Catalytically activated palladium@platinum nanowires for accelerated hydrogen gas detection. ACS Nano *9*, 3215–3225.
10. Jung, W.B., Cho, S.-Y., Suh, B.L., Yoo, H.-W., Jeon, H.-J., Kim, J., and Jung, H.-T. (2019). Polyelemental nanolithography via plasma ion bombardment: From fabrication to superior H_2 sensing application. Adv. Mater. *31*, 1805343.
11. Hughes, R., and Schubert, W. (1992). Thin films of Pd/Ni alloys for detection of high hydrogen concentrations. J. Appl. Phys. *71*, 542–544.
12. Hassan, K., Uddin, A.I., and Chung, G.-S. (2016). Fast-response hydrogen sensors based on discrete Pt/Pd bimetallic ultra-thin films. Sens. Actuators, B *234*, 435–445.
13. Lim, B., Jiang, M., Camargo, P.H.C., Cho, E.C., Tao, J., Lu, X., Zhu, Y., and Xia. Y. (2009). Pd-Pt bimetallic nanodendrites with high activity for oxygen reduction. Science *324*, 1302–1305.
14. Wang, D., and Li, Y. (2011). Bimetallic nanocrystals: Liquid-phase synthesis and catalytic applications. Adv. Mater. *23*, 1044–1060.
15. Cortie, M.B., and McDonagh, A.M. (2011). Synthesis and optical properties of hybrid and alloy plasmonic nanoparticles. Chem. Rev. *111*, 3713–3735.
16. Ferrando, R., Jellinek, J., and Johnston, R.L. (2008). Nanoalloys: From theory to applications of alloy clusters and nanoparticles. Chem. Rev. *108*, 845–910.
17. Yang, F., Donavan, K.C., Kung, S.-C., and Penner, R.M. (2012). The surface scattering-based detection of hydrogen in air using a platinum nanowire. Nano Lett. *12*, 2924–2930.
18. Kobayashi, H., Yamauchi, M., Kitagawa, H., Kubota, Y., Kato, K., and Takata, M. (2010). Atomic-level Pd−Pt alloying and largely enhanced hydrogen-storage capacity in bimetallic nanoparticles reconstructed from core/shell structure by a process of hydrogen absorption/desorption. J. Am. Chem. Soc. *132*, 5576–5577.
19. Burda, C., Chen, X., Narayanan, R., and El-Sayed, M.A. (2005). Chemistry and properties of nanocrystals of different shapes. Chem. Rev. *105*, 1025–1102.
20. Xia, Y., Xiong, Y., Lim, B., and Skrabalak, S.E. (2009). Shape-controlled synthesis of metal nanocrystals: Simple chemistry meets complex physics? Angew. Chem., Int. Ed. *48*, 60–103.
21. Ying, J., Yang. X.-Y., Hu, Z.-Y., Mu, S.-C., Janiak, C., Geng, W., Pan, M., Ke, X., Tendeloo, G.V., and Su, B.-L. (2014). One particle@one cell: highly monodispersed PtPd bimetallic nanoparticles for enhanced oxygen reduction reaction. Nano Energy *8*, 214–222.

22. Esparza, R., Santovena, A., Ruiz-Baltazar, A., Angeles-Pascual, A., Bahena, D., Maya-Cornejo, J., Ledesma-Garcia, J., and Perez, R. (2017). Study of PtPd bimetallic nanoparticles for fuel cell applications. Mater. Res. *20*, 1193–1200.
23. Liu, J., Yin, J., Feng, B., Li, F., and Wang, F. (2019). One-pot synthesis of unprotected PtPd nanoclusters with enhanced catalytic activity, durability, and methanol-tolerance for oxygen reduction reaction. (2019). Appl. Surf. Sci. *473*, 318–325.
24. Yang, X., Yang, Q., Xu, J. and Lee, C.-S. (2012). Bimetallic PtPd nanoparticles on Nafion–graphene film as catalyst for ethanol electro-oxidation. J. Mater. Chem. *22*, 8057–8062.
25. Censabella, M., Torrisi, V., Boninelli, S., Bongiorno, C., Grimaldi, M.G., and Ruffino, F. (2019). Laser ablation synthesis of mono- and bimetallic Pt and Pd nanoparticles and fabrication of Pt-Pd/graphene nanocomposites Appl. Surf. Sci. *475*, 494–503.
26. Rifai, S., Breen, C.A., Solis, D.J., and Swager, T.M. (2006). Facile in situ silver nanoparticle formation in insulating porous polymer matrices. Chem. Mater. *18*, 21–25.
27. Kim, Y., Moh, L.C., and Swager, T.M. (2017). Anion exchange membranes: Enhancement by addition of unfunctionalized triptycene poly(ether sulfone)s. ACS Appl. Mater. Interfaces *9*, 42409–42414.
28. Koo, W.-T., Kim, Y., Savagatrup, S., Yoon, B., Jeon, I., Choi, S.-J., Kim, I.-D., and Swager, T.M. (2019). Porous ion exchange polymer matrix for ultrasmall Au nanoparticle-decorated carbon nanotube chemiresistors. Chem. Mater. *31*, 5413–5420.
29. Tsui, N.T., Paraskos, A.J., Torun, L., Swager, T.M., and Thomas, E.L. (2006). Minimization of internal molecular free volume: A mechanism for the simultaneous enhancement of polymer stiffness, strength, and ductility. Macromolecules *39*, 3350–3358.
30. Zhou, L.-N., Zhang, X.-T., Wang, Z.-H., Guo, S., and Li, Y.-J. (2016). Cubic superstructures composed of PtPd alloy nanocubes and their enhanced electrocatalysis for methanol oxidation. Chem. Commun. *52*, 12737–12740.
31. Schiavo, L., Aversa, L., Tatti, R., Verucchi, R., and Carotenuto, G. (2016). Structural characterizations of palladium clusters prepared by polyol reduction of $[PdCl_4]^{2-}$ ions. J. Anal. Methods Chem. *2016*, 9073594.
32. van Wyk, P.-H., Gerber, W.J., and Koch, K.R. (2011). A robust method for speciation, separation and photometric characterization of all $[PtCl_{6-n}Br_n]^{2-}$ (n= 0–6) and $[PtCl_{4-n}Br_n]^{2-}$ (n= 0–4) complex anions by means of ion-pairing RP-HPLC coupled to ICP-MS/OES, validated by high resolution ^{195}Pt NMR spectroscopy. Anal. Chim. Acta *704*, 154–161.
33. Gigola, C.E., Moreno, M.S., Costilla, I., and Sanchez, M.D. (2007). Characterization of Pd–CeO_x interaction on α-Al_2O_3 support. Appl. Surf. Sci. *254*, 325–329.
34. Jerdev, D.I., and Koel, B.E. (2002). Fe deposition on Pt (111): A route to Fe-containing Pt–Fe alloy surfaces. Surf. Sci. *513*, L391–L396.
35. Zhang, G., Huang, C., Qin, R., Shao, Z., An, D., Zhang, W., and Wang, Y. (2015). Uniform Pd–Pt alloy nanoparticles supported on graphite nanoplatelets with high electrocatalytic activity towards methanol oxidation. J. Mater. Chem. A *3*, 5204–5211.
36. Chang, J., Feng, L., Liu, C., Xing, W., and Hu, X. (2014). Ni_2P enhances the activity and durability of the Pt anode catalyst in direct methanol fuel cells. Energy Environ. Sci. *7*, 1628–1632.
37. Koo, W.-T., Cha, J.-H., Jung, J.-W., Choi, S.-J., Jang, J.-S., Kim, D.-H., and Kim, I.-D. (2018). Few-layered WS_2 nanoplates confined in Co, N-doped hollow carbon nanocages: Abundant WS_2 edges for highly sensitive gas sensors. Adv. Funct. Mater. *28*, 1802575.
38. Thomason, M.J., Seabourne, C.R., Sattelle, B.M., Hembury, G.A., Stevens, J.S., Scott, A.J., Aziz, E.F., and Schroeder, S.L.M. (2015). Self-association of organic solutes in solution: A NEXAFS study of aqueous imidazole. Faraday Discuss. *179*, 269–289.
39. Joo, S.H., Park, C., Kim, E.A., Lee, Y.H., Chang, H., Seung, D., Choi, Y.S., Park, J.-B., and Kim, T.K. (2008). Functionalized carbon nanotube-poly(arylene sulfone) composite membranes for direct methanol fuel cells with enhanced performance. J. Power Sources *180*, 63–70.
40. Guilera, G., Newton, M.A., Polli, C., Pascarelli, S., Guino, M., and Hii, K.K. (2006). In situ investigation of the oxidative addition in homogeneous Pd catalysts by synchronised time resolved UV-Vis/EXAFS. Chem. Commun. *41*, 4306-4308.
41. Knecht, M.R., Weir, M.G., Myers, V.S., Pyrz, W.D., Ye, H., Petkov, V., Buttrey, D.J., Frenkel, A.I., and Crooks, R.M. (2008). Synthesis and characterization of Pt dendrimer-encapsulated nanoparticles: effect of the template on nanoparticle formation. Chem. Mater. *20*, 5218-5228.
42. Kim, Y., Zhu, J., Yeom, B., Prima, M.D., Su, X., Kim, J.-G., Yoo, S.J., Uher, C., and Kotov, N.A. (2013). Stretchable nanoparticle conductors with self-organized conductive pathways. Nature *500*, 59–63.
43. Kim, D.-H., Kim, S.-J., Shin, H., Koo, W.-T., Jang, J.-S., Kang, J.-Y., Jeong, Y.J., and Kim, I.-D. (2019). High-resolution, fast, and shape-conformable hydrogen sensor platform: Polymer nanofiber yarn coupled with nano-grained Pd@Pt. ACS Nano *13*, 6071–6082.
44. Yoo, H.-W., Cho, S.-Y., Jeon, H.-J., and Jung, H.-T. (2015). Well-defined and high resolution Pt nanowire arrays for a high performance hydrogen sensor by a surface scattering phenomenon. Anal. Chem. *87*, 1480–1484.
45. Cho, S.-Y., Ahn, H., Park, K., Choi, J., Kang, H., and Jung, H.-T. (2018). Ultrasmall grained Pd nanopattern H_2 Sensor. ACS Sens. *3*, 1876–1883.
46. Shim, Y.-S., Jang, B., Suh, J.M., Noh, M.S., Kim, S., Han, S.D., Song, Y.G., Kim, D.H., Kang, C.-Y., Jang, H.W. et al. (2018). Nanogap-controlled Pd coating for hydrogen sensitive switches and hydrogen sensors. Sens. Actuators, B *255*, 1841–1848.
47. Jang, J.-S., Qiao, S., Choi, S.-J., Jha, G., Ogata, A.F., Koo, W.-T., Kim, D.-H., Kim, I.-D., and Penner, R.M. (2017). Hollow Pd–Ag Composite nanowires for fast responding and transparent hydrogen sensors. ACS Appl. Mater. Interfaces *9*, 39464–39474.
48. Lim, M.A., Kim, D.H., Park, C.-O., Lee, Y.W., Han, S.W., Li, Z., Williams, R.S., and Park, I. (2011). A new route toward ultrasensitive, flexible chemical sensors: metal nanotubes by wet-chemical synthesis along sacrificial nanowire templates. ACS Nano *6*, 598–608.

49. Hassan, K., and Chung, G.-S. (2017). Fast and reversible hydrogen sensing properties of Pd-capped Mg ultra-thin films modified by hydrophobic alumina substrates. Sens. Actuators, B *242*, 450–460
50. Fahad, H.M., Shiraki, H., Amani, M., Zhang, C., Hebbar, V.S., Gao, W., Ota, H., Hettick, M., Kiriya, D., Chen, Y.-Z. et al. (2017). Room temperature multiplexed gas sensing using chemical-sensitive 3.5-nm-thin silicon transistors. Sci. Adv. *3*, e1602557.
51. Ndaya, C.C., Javahiraly, N., and Brioude, A. (2019). Recent advances in palladium nanoparticles-based hydrogen sensors for leak detection. Sensors *19*, 4478.
52. Yoo, S.J., Park, H.-Y., Jeon, T.-Y., Park, I.-S., Cho, Y.-H., and Sung, Y.-E. (2008). Promotional effect of palladium on the hydrogen oxidation reaction at a PtPd alloy electrode. Angew. Chem. Int. Ed. *47*, 9307–9310.
53. Weng, Y.-C., and Hsieh, C.-T. (2011). Scanning electrochemical microscopy characterization of bimetallic Pt–M (M= Pd, Ru, Ir) catalysts for hydrogen oxidation. Electrochim. Acta *56*, 1932–1940.
54. Kodchakorn, K., Lee, V.S., Yana, J., and Nimmanpipug, P. Density functional theory calculations of hydrogen dissociative adsorption on platinum-involved alloy surfaces. Surf. Coat. Technol. *306*, 35-40.
55. Zhu, R., Desroches, M., Yoon, B., and Swager, T.M. (2017). Wireless oxygen sensors enabled by Fe(II)-polymer wrapped carbon nanotubes. ACS Sens. *2*, 1044–1050.
56. Ruiz-Garcia, L., Lunadei, L., Barreiro, P., and Robla, J.I. (2009). A Review of Wireless Sensor Technologies and Applications in Agriculture and Food Industry: State of the Art and Current Trends. Sensors *9*, 4728–4750.